Proceedings of IMECE2002:
2002 ASME International Mechanical Engineering Congress and Exposition
New Orleans, Louisiana, November 17–22, 2002

IMECE2002-33171

FUNDAMENTAL ISSUES AND LATEST DEVELOPMENT IN HOLOGRAPHIC PARTICLE IMAGE VELOCIMETRY

Ye Pu
Laser Flow Diagnostics Lab
Dept. of Mech. & Aero. Eng.
SUNY at Buffalo
Buffalo, NY 14260

Lujie Cao
Laser Flow Diagnostics Lab
Dept. of Mech. & Aero. Eng.
SUNY at Buffalo
Buffalo, NY 14260

Hui Meng
Laser Flow Diagnostics Lab
Dept. of Mech. & Aero. Eng.
SUNY at Buffalo
Buffalo, NY 14260

ABSTRACT

Holographic PIV (HPIV) is currently the most promising technique for truly instantaneous, three-dimensional (3D), three-component (3C) velocity field measurements for complex flows including turbulent and multiphase flows. This paper reports new understanding on some fundamental issues and challenges in HPIV including the complex 3D imaging characteristics, the extraction of full particle information (intensities, sizes, and locations) in 3D space, the extraction of particle displacements, and the huge data volume to process. The latest off-axis HPIV system will be presented, which incorporates the new understanding of imaging characteristics of particle holography, careful development of data processing algorithms, and a well-designed distributed parallel processing system. We will demonstrate capabilities of HPIV by a semi-time-series measurement of instantaneous 3D, 3C velocity fields in highly 3D vortical flow.

INTRODUCTION

Turbulent flow is a highly complex and yet ubiquitous physical phenomenon that we know very little about. The understanding, modeling, and control of turbulence requires proper experimental tools to reveal the fluctuating three-dimensional (3D) vorticity at a wide range of time and length scales, which has posed an overwhelming challenge to modern technology in many aspects. The recently matured Particle Image Velocimetry (PIV) technique only partially fulfills this need by providing two-component (2C) [1,2] or three-component (3C) [3,4] velocity measurement on a two-dimensional (2D) plane. Further explorations [5,6] attempted to expand PIV capabilities to cover a volumetric domain by rapidly scanning the volume plane by plane. However, instantaneous full- field 3D measurement with sufficient spatial resolution and dynamic range is beyond the reach of conventional PIV.

Holographic Particle Image Velocimetry (HPIV) is a full-field, instantaneous, 3D flow diagnostics tool that holds the promise to provide heretofore-unavailable detailed experimental data in turbulent flows. In-line holography has traditionally attracted intensive research interest and wide applications [7,8,9,10,11] because of its experimental simplicity and low equipment requirement. However, due to its excessive intrinsic speckle noise in the reconstructed image [12], in-line holography was restricted to measurements of sparsely dispersed particles [10,11]. Thus recent development in HPIV has concentrated on off-axis holography, where the reference waves are introduced at an angle with the object wave. Off-axis HPIV shows significantly improved imaging signal-to-noise ratio (SNR) over the in-line versions and allows much higher seeding densities [13,14]. Indeed, most of the recent successful works in HPIV are based on off-axis holography [13,14,15,16].

Despite the previous research efforts and successes, fundamental knowledge about the science of HPIV is still rather limited. In particular, our understanding about the imaging characteristics of particle holography is still at a rudimentary level. Often, it is assumed that the hologram reconstructs a spherical wave converging to the center of the particle [17]. None of the reported HPIV systems has taken into account the complex nature of Mie-scattering [18] in its design. Furthermore, the exact signal-noise characteristics in off-axis HPIV with regard to relevant parameters is lacking, although Meng et al. offered a thorough analysis on the same phenomena for in-line HPIV [12]. The lack of such knowledge hinders the objective justification of a particular design and the reliable estimation of its accuracies and capabilities.

In this paper, we present our new understanding in the physics of particle holography, from which we derive a systematic method for predicting the capacity limits and measurement accuracies of HPIV from system parameters. The application of such method helps the optical design of HPIV systems. Such analyses have enabled us to provide a detailed, quantitative specification for our own HPIV system. Our research shows that imperfect 3D particle images formed by the wavefront reconstruction of the light scattering from small particles and the associated speckle noises hold the primary responsibility for the theoretical limits in accuracy and capacity of HPIV. These two issues are *intrinsic* to the physical process in HPIV. Their negative effects can only be alleviated by better choices of system parameters but never be eliminated. Using results from our simulation and theoretical analyses, we discuss the basic optical configurations of HPIV. Further details in these works are left for later, more focused publications. Finally, we demonstrate our latest development in HPIV technology with a semi-time-series measurement of a flow passing a wall-mounted tab, which revealed a phase-locked sequence of a vortex shedding process in a complete cycle.

BASIC OFF-AXIS HPIV CONFIGURATIONS

Because of the importance of the scattering phenomena in off-axis HPIV, we categorize HPIV configurations by the recording angle θ_H, i.e. the angle between the normal vector $\mathbf{n}_H$ of the recording plane H and the propagation vector $\mathbf{k}_i$ of the object-illuminating light. Thus there are three major categories of HPIV configurations: forward (or near-forward) recording ($\theta_H \approx 0°$), backward (or near backward) recording ($\theta_H \approx 180°$), and 90-degree recording ($\theta_H \approx 90°$).

Figure 1 illustrates these HPIV configurations, while also stressing the critical role of polarization. The angle between each reference beam and $\mathbf{n}_H$ is α_r. Based on the polarizations of the reference and object waves, 90-degree recording is further classified as vertical-polarization configuration, where the polarization of the object wave and the reference waves are parallel everywhere, and horizontal-polarization configuration, where the polarizations of the object wave and the reference waves are not parallel to each other but share a parallel component.

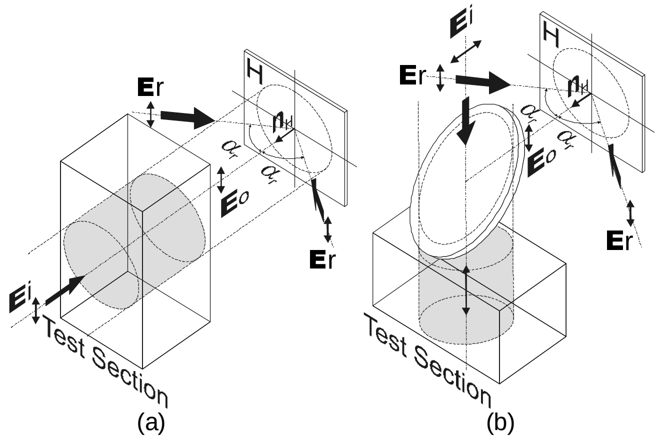

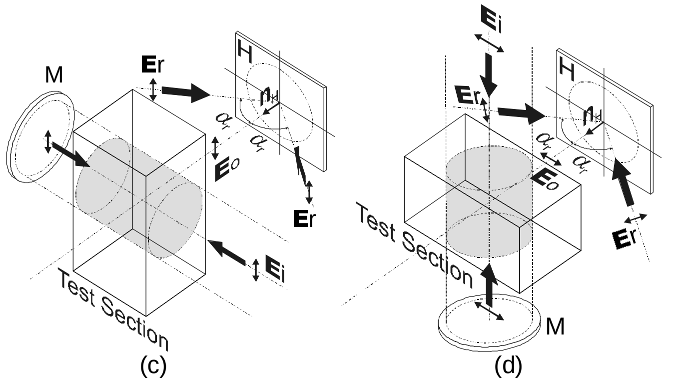

Figure 1. Optical configurations for off-axis, dual-reference-beam HPIV. (a) Forward scattering. (b) Backward scattering. (c) 90-degree scattering, vertical-polarization configuration. (d) 90-degree, horizontal-polarization configuration. **E**i: illuminating wave. **E**r: reference wave. α_r: reference angle. $\mathbf{n}_H$: normal vector of holographic plane. M: mirror.

Even for perfect holograms, simulations based on Mie-scattering theory show that complicated aberrations result in all scattering directions for finite particle sizes. The aberrations degrade the signal integrity and cause bodily shifts in the reconstructed images. Among the three configurations, forward and backward recording produce large spherical aberrations and apparent image shifts along the optical axis ($\mathbf{n}_H$) as much as 1.5 and 3 times of particle diameter (d_p), respectively. 90-degree recording produces astigmatism in the reconstructed images, which results in an apparent shift of about $0.25d_p$ in the transverse direction (the direction perpendicular $\mathbf{n}_H$). In all configurations smaller particles produces much less aberrations.

Optical access at non-orthogonal angles is certainly possible. However, without special optical treatment, liquid fluid media and flow facility walls will cause severe aberrations and seriously damage the signal integrity.

The SNR of the reconstructed particle images is a monotonic function of $I_0 / \langle I_N \rangle$, where I_0 is the intensity of the particle image, and $\langle I_N \rangle$ is the mean noise intensity. Our theoretical analysis suggests that the optimum value of $I_0 / \langle I_N \rangle$ (assuming reconstruction of a perfect spherical wave) in the reconstructed image is

$$\frac{I_0}{\langle I_N \rangle} = \frac{\pi \tan^2 \Omega}{\lambda^2 n_s L}, \tag{1}$$

where Ω is the imaging angular aperture (limited by the aperture of either the hologram or the camera, whichever is smaller), λ is the wavelength, n_s the seeding number density, and L the depth of the illuminated volume (the dimension along $\mathbf{n}_H$). Clearly, the angular aperture of the hologram is a critical design parameter to achieve high image SNR. Among the three

HPIV configurations, forward recording has the smallest angular aperture yet the strongest intensity.

We must bear in mind that, with optical reconstruction, mechanical misalignment and vibration during the scanning always exists. Furthermore, the shrinkage of the holographic emulsion due to chemical processing also drastically degrades the reconstructed images and introduces measurement error. We deem it the ultimately desirable solution to capture the holographic fringes directly with very-high-resolution electronic devices and reconstruct the 3D image field numerically.

CAPABILITY LIMITS OF HPIV

Two factors set the basic boundaries in HPIV measurement: seeding density, which determines the spatial data sampling rate, and particle centroid uncertainty, which sets the primary limit in the accuracy and dynamic range of the measurement. Given a proper off-axis holographic recording and the minimum SNR required by a particular algorithm for correct extraction of particle positions, the intrinsic speckle noise is the essential limiting factor for the maximum achievable seeding density.

For given recording and interrogation conditions and the minimum SNR required for the extraction of useful information, we find the following requirement must be satisfied:

$$n_s L \le \frac{\pi \gamma \tan^2 \Omega}{\mathscr{M} \lambda^2 \left(I_0 / \langle I_N \rangle \right)_{\min}}, \tag{2}$$

where $\mathscr{M}$ is the ratio of the pixel size to the mean speckle size [19], and γ the signal integrity defined as the ratio of the actual focal image intensity to the focal intensity of a spherical wave with the same amount of light energy. The value of γ is closely related to the scattering characteristics ($0 < \gamma < 1$).

Equation 2 sets an upper limit of number density of particles given a minimum SNR requirement. Notice that seeding density n_s appears in a product with the axial depth of the test volume L. Thus given the HPIV configuration and SNR requirement, higher spatial resolution can be achieved at the expense of reduced depth of the test volume.

Next, we estimate the range of Reynolds number (*Re*) within which HPIV can resolve the full spectrum of flow structures. The number density of seeding particles determines the spatial resolution and hence the size of the smallest flow structures resolvable, while the depth of the test volume L determines the largest eddy size that the measurement can capture. For uniform particle dispersion, we take the mean free distance between particles as the smallest eddy size: $\eta = (3/4\pi n_s)^{1/3}$. If L is the integral length scale and η the Kolmogorov length scale, the maximum Reynolds number resolvable in HPIV measurement is [20]

$$Re_{\max} = \left(\frac{L}{\eta} \right)^{\frac{4}{3}} = \left(\frac{4\pi n_s L^3}{3} \right)^{\frac{4}{9}}. \tag{3}$$

The uncertainty in the reconstructed particle position (ε_p) is specific to the optical setup, particle size, particle relative refractive index, and the specific algorithm to extract the particle position. For uniform particle sizes, the system error due to Mie scattering and holography process does not significantly impact the centroid accuracy. If the particle size is non-uniform, the uncertainty in particle size is translated into the uncertainty of the centroid position.

The flow velocity extracted from displacement (Δx) between particles in the double exposures and the time interval (Δt) inherits its uncertainty (ε_v) from the uncertainty in the particle positions (ε_p). Yet, uncertainties in Δt are negligible owing to the ps accuracy in typical modern pulsed lasers. Thus, for velocities obtained from individually paired particles,

$$\varepsilon_v = \sqrt{\varepsilon_p^2 + \varepsilon_p^2} \Big/ \Delta t = \sqrt{2}\, \varepsilon_p \Big/ \Delta t, \tag{4}$$

At a cost of lowered velocity spatial resolution, though, calculating the mean velocity from a group of N particles reduces this uncertainty to $1/\sqrt{N}$, i.e.

$$\varepsilon_v = \sqrt{\frac{2}{N}}\, \varepsilon_p \Big/ \Delta t \cdot \tag{5}$$

The above estimation also applies to velocities obtained through correlation, which are essentially mean velocities of particle groups. The dynamic range of the velocity is $v_{\max} / \varepsilon_v$, where v_{max} is the maximum velocity that a particular algorithm is able to resolve.

Quantities related to velocity derivatives bear more uncertainties because data at multiple points in space are involved. For example, computing vorticity through simple finite difference at a particular point involves six adjacent data points. Computing divergence takes the same amount of data points in a slightly different fashion. Since these higher-order quantities involve again linear operations over the original data, the above analysis for uncertainties in the velocities applies. Therefore,

$$\varepsilon_D = \varepsilon_\omega = \sqrt{6}\, \varepsilon_v \big/ 2 s_g, \tag{6}$$

where ε_D is the uncertainty in divergence, ε_ω the uncertainty in vorticity, and s_g the grid spacing. Equation 4 suggests that the uncertainty in the velocity contributes approximately the same amount of uncertainty to the divergence and to the vorticity. For incompressible flows, ε_D. is the residue divergence and can be conveniently used to estimate the uncertainty in the vorticity.

Analyses show that the velocity gradients are the primary cause of failures in the extraction of velocity through correlation techniques. The reason for these failures is that the geometrical (morphological) pattern formed by all particles participating the correlation changes between double exposures due to the velocity gradients. Fundamentally, correlations are shift-and-match processes vulnerable to pattern deformations. The maximum resolvable vorticity is determined by the maximum deformation Δ_m that a specific velocity extraction algorithm can handle. The vorticity is related to these deformations through $\omega = 2\sigma_x / D\Delta t$, where D is the size of the IC, and σ_x is the pattern deformation (defined as the standard deviation of all particle coordinates). Uncertainties in the particle positions also cause morphological deformations, which, as far as the correlation algorithm are concerned, is completely indistinguishable from the real deformations. Hence, the actual maximum tolerable deformation is Δ_m - ε_p. The dynamic range of the measurable vorticity is then

$$\frac{\omega_{\max}}{\omega_{\min}} = \frac{2(\Delta_m - \varepsilon_p)/D\Delta t}{\varepsilon_\omega}. \tag{7}$$

THE GEMINI HPIV SYSTEM

Over the past few years, we have developed a complete HPIV instrument, Gemini, which employs 90-degree scattering off-axis holography configuration. The system consists two major components: holographic recording/reconstruction subsystem, and data processing subsystem. In the following, we describe this system in its optical configuration, data processing algorithms, and distributed parallel computing cluster.

Optical configuration

We have reported the optical configuration of the holographic recording/reconstruction subsystem in the Gemini HPIV system in [13]. The system uses an injection-seeded, dual-cavity Nd:YAG laser (Spectra-Physics PIV-400) for both recording and reconstruction. The laser gives a pair of temporally and spatially separated laser pulses, each of 8ns duration. As in regular PIV applications, the pulse separation Δt is adjusted according to the estimated flow speed. The holographic recording step follows a dual-reference approach, which provides angular separation of the reference beams for the double-exposure hologram, so that the two holographic images can be reconstructed independently on one hologram. The Gemini HPIV system is capable of accommodating both the vertical- and the horizontal-polarization configurations in Figure 1 (c) and (d).

To minimize aberrations, exactly the same laser and reference beams used for recording are employed for reconstruction. The frozen 3D particle images from each exposure are reconstructed on-demand and interrogated via 3D scanning. A Pentium personal computer controls the scanning mechanism (a 3D traverse system) and the data acquisition. This computer serves as the acquisition node in a distributed computing environment, as well as a stand-alone processing power if no parallel computing facility is available. The acquisition node instructs the 3D traverse system to locate the camera at requested locations, capture the reconstructed images, and then either dispatch the image data to processing nodes or perform the processing by itself if necessary.

Processing algorithms

In [13] we have implemented a Concise Cross Correlation (CCC) algorithm that correlates and tracks 3D particle movement with discrete particle centroid coordinates. CCC consists of two steps: correlation and pairing. The correlation operation is responsible for finding the mean displacements between the two groups of centroids, while the pairing operation is responsible for mapping individual centroid movement. We decompose the 3D correlation into three 1D correlations performed in space domain: keeping one centroid set fixed in its original place, we translate the other set in space and compute their correlation function. The displacement yielding the highest correlation peak is considered the translation of the particle group and is the correlation output. After the translation of particle groups is extracted, CCC individually pairs each particle based on the information obtained from the first step and a shortest distance classification criterion. Numerical simulations show that CCC handles velocity gradients much better than traditional 3D FFT-based correlation [21].

Both simulations and experience from experiments [22] show that the holographically reconstructed particle images involve extremely complex 3D morphology, which, combined with the speckle noise, poses a great challenge to the retrieval of the particle information. This problem is especially severe when full particle information is needed for categorization in multiphase flow measurement. Therefore, we further implemented the Particle Reconstruction by Edge Detection (PRED) algorithm, which extracts the continuous 3D exterior surface of a particle image based on 2D edge detection and recursive 3D labeling [21]. This more complete and more accurate particle information, however, comes at an expense of processing time: PRED is up to five times slower compare to the previous simpler algorithm introduced in [14].

Distributed parallel processing

Processing of HPIV data (extraction of information from 3D particle images) represents a major challenge in the development of practical HPIV instruments. The vast amount of image data (often more than 100GB of raw image data per hologram) takes more than 50 hours for a single 600MHz Pentium grade computer to process just one snapshot. Experiments involving multiple snapshots can produce tens or even hundreds of holograms. This memory- and computation-intensive task calls for a parallel computing architecture to bring the total processing time down to a few hours.

A distributed parallel computing system constitutes the best choice for HPIV data processing, where multiple computers are interconnected with high-speed communication network and jointly process a common task in parallel. Such a system provides computing power comparable to high-end commodity massive parallel processors at a fraction of the cost. Furthermore, its flexibility and the use of mainstream commodity equipments drastically simplify the programming, maintenance, and upgrade tasks compared with an application-specific, hardware-based solution.

Based on an initial effort [23] experimenting a parallel version of the processing algorithm, we have recently built such a computing infrastructure with commodity Pentium PCs connected by a high-speed, low-latency Myrinet network to satisfy the computing need. Owing to the on-board communication processor in the Myrinet network interface, intensive communication task is off-loaded from the main processor in each computing node, making the computing and acquisition operations largely overlapped with the communication.

Figure 2 depicts the hardware infrastructure of the distributed parallel processing system. The acquisition node controls the 3D traverse system to scan the 3D image volume and acquires image data from the digital camera. After image data for one interrogation cell (IC) is collected, the acquisition computer dispatches the data to one of the processing nodes through the Myrinet switch. The 1.28Gb/sec data rate of Myrinet guarantees prompt and efficient distribution of image data among the processing nodes. The processing nodes send the results back to the acquisition node after they finish their tasks.

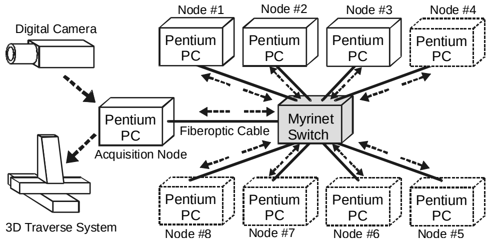

Figure 2. Hardware infrastructure of the distributed parallel computing cluster in Gemini HPIV system. The current system implemented the acquisition node and three processing nodes.

The software architecture is based on a master-slave model, with the program running on the acquisition node serving as the master and the programs running on the processing nodes serving as slaves. We use the standard message-passing interface (MPI) for inter-process communication support. The master process continuously scans (through the traverse system) the 3D image field one IC after another and dispatch the acquire image slices to the slave process, which is a MPI program implementing PRED and CCC algorithm.

System Specification

We now analyze the capacity of the Gemini system based on previous discussions. The angular aperture (half cone angle) of this 90-degree scattering, off-axis HPIV system depends on the distance from the test section to the hologram, the effective hologram size, and whether a relay lens is used. The sampling pixel size used for reconstruction image interrogation is 4μm, which corresponds to $\mathscr{M} \approx 3$. We estimate that the signal integrity $\gamma = 0.5$ for 10μm particles (glass spheres in water). To achieve $SNR_{min} = 5$, $\left[I_0 / \langle I_N \rangle\right]_{\min} \approx 50$. In one experimental setup, we used $\Omega = 8.5^{\circ}$. According to Equation 2, the seeding density limit is $n_s L \leq 826 mm^{-2}$, which corresponds to a maximum allowable seeding density of $n_s = 20$ particles per mm^3 for a 40mm depth of volume. This density gives a spatial resolution of $\eta = 0.23$mm, thus from Equation 3 we estimate $Re_{\max} \approx 970$ in order to resolve the smallest and the largest eddies simultaneously. For flows at higher Re values, the full range of flow structures cannot be resolved. In another experimental setup, an angular aperture of 15° was used, corresponding to a density limit of $n_s L \leq 2656 mm^{-2}$. For the same depth of volume the maximum allowable seeding density is $n_s = 66$ particles per mm^3. This density allows us to measure flows up to $Re_{\max} \approx 1700$. As a comparison, forward-scattering holography with 10μm particles has an angular aperture of about 3.5° determined by diffraction, which requires $n_s L \leq 138 mm^{-2}$ and allows only 3.5 particles per mm^3 for $L = 40$mm. This would limit the flow to $Re_{\max} \approx 460$.

The measurement accuracy of the system depends on the seeding particles used in the measurement. A typical kind of particles used in our experiments is TSI 10089 hollow glass sphere (size range 5μm < d_p < 14μm, relative refractive index $m = 1.15$). In 90-degree scattering at this relative refractive index, simulations based on Mie-theory show that the centroid error due to the optical process is about $0.25 d_p$; hence in this case the optical uncertainty is less than 1.2μm. In forward scattering, as a comparison, the optical uncertainty for the same type of particles would be 7.2μm. It is worth pointing out that, when the holographic reconstruction and data processing involves mechanical scanning and alignment, the mechanical precision is of vital importance. The misalignment and vibrations [24] often dominates the uncertainty in the final results.

The dynamic ranges can be found from the capability of the extraction algorithms and the measurement uncertainty in particle positions. Monte Carlo simulations show that our algorithm has an uncertainty of 10μm in axial direction (the worst direction in terms of accuracy), which actually dominates the final uncertainty in the particle centroid without regard to errors due to mechanical scanning. Our particle displacement extraction algorithm (CCC) tolerates translations more than 1/3 of the IC size under usual conditions (moderate velocity gradients). For IC of 4mm×4mm×4mm in size sampled with 4µm pixels, the maximum translation measurable is about 1,200µm, which projects to a dynamic range of 120. On the other hand, the *measured* uncertainty in the particle centroid is approximately 40µm, a major portion of which comes from mechanical vibrations and misalignments. Thus at present the velocity dynamic range is about 30. Electronic holographic image sensors (though presently have not achieved resolutions required by off-axis holography) will eliminate the mechanical scanning errors and could boost the velocity dynamics to 120. It should be pointed out that, with higher laser power, the use of smaller seeding particles (1µm diameter, for example) can drastically improve the optical integrity of the reconstructed images and grossly boost the accuracy in the particle positions and thus the velocity dynamic range. The estimated velocity uncertainty, assuming a grid spacing s_g = 1mm during interpolation and a seeding density of 10 particles per mm^{-3}, is about $12\mu m/\Delta t$. Furthermore, quantitative calibrations show that CCC algorithm tolerates a maximum deformation of $\Delta_m = 0.2D$, which, according to Equation 5, leads to a vorticity dynamic range of 96. This rather large vorticity dynamic range is a result of CCC algorithm's capability of handling large velocity gradients.

A SEMI-TIME-SERIES HPIV MEASUREMENT

To provide both temporally and spatially resolved 3D velocity measurements have always been the ultimate goal for HPIV. With the Gemini HPIV system and the implementation of the enhanced processing system, for the first time this goal has become tangible. However, the lack of a proper recording media transport system at the present stage prevents us from carrying out such type of measurements. To demonstrate the capability of the Gemini HPIV system, we instead perform a semi-time-series, phase-locked measurement of a flow passing a wall-mounted tab, where the measurement is phase-locked with the flow phenomena, and the dynamics of the coherent structure is revealed at a sequence of phases.

To phase-lock the coherence structure of the flow with the laser pulses, we first build an "active" tab, which is driven through a linear solenoid. With proper driving signal to the solenoid, the tab introduces a small amount of disturbances to the flow at the tab tip. The disturbances are precisely synchronized with the laser pulses at a frequency very close to the natural frequency of the vortex shedding, so that the coherent structure of the flow will be "attracted" to the excitation frequency and synchronized to the laser pulses. With proper delay between the disturbances and the laser pulses, we can record the flow structure at different phases. Because the natural frequency of the tab wake is much lower than the frequency of the laser pulses (10Hz), we use a dividing delay generator to produce the driving signal so that the disturbances introduced to the flow is a sub-harmonic of the laser frequency. LDV measurement shows that the flow has a natural frequency of 1.3Hz. Using the closest sub-harmonic of the laser frequency 1.25Hz as excitation, we are able to phase-lock the flow.

Flow visualizations show that the flow is properly phase-locked with the controlled excitation. Figure 3 (a) demonstrates the average intensity of 100 frames of flow visualization images of the "natural" flow without excitation. No flow structure is identifiable since structures at different phases cancel out. Figure 3 (b) shows the averaged image of the phase-locked flow with excitation where the coherent structures are clearly identifiable.

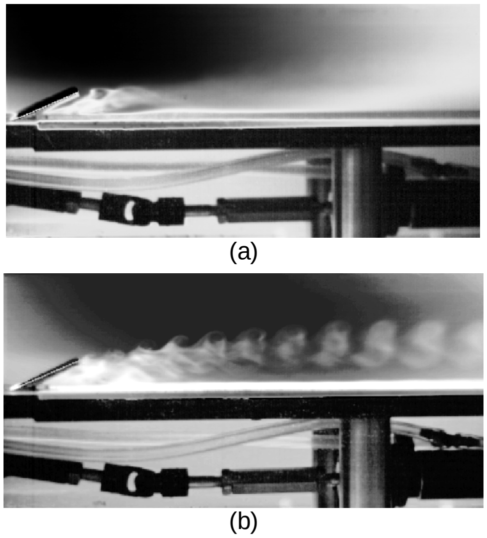

Figure 3. Validation of phase lock by flow visualization and LDV measurement. (a) Intensity average from 100 frames of flow visualization images without phase lock. (b) Intensity 100 frames of flow visualization images with phase lock.

Shown in Figure 4 is the optical setup for the flow measurement. Due to the large size and the horizontal orientation of the test section, which is a part of a 6" recirculating water tunnel, we have to introduce the illuminating beam from the top. Therefore, unlike our previous HPIV measurement [14] where the test section was vertical, here we are dealing with the less preferred horizontal-polarization configuration. To counter the decreased fringe visibility in this type of configuration, we use fixation-free bleaching (Ferric EDTA III) [25] in the chemical processing of the hologram for better diffraction efficiency and minimal emulsion shrinkage (which is one of the major causes for aberrations in practical holography).

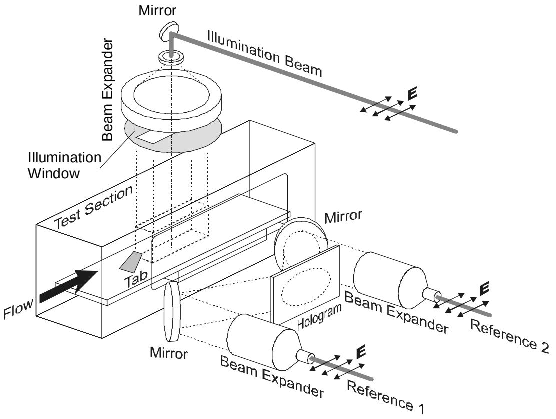

Figure 4. Optical setup for the phase-locked measurement of flow passing a wall-mounted tab. Note that horizontal-polarization configuration is used due for optical access.

The centroid uncertainty is highly specific to the optical configuration. We calibrate this experimental setup by holographically recording standard 10μm particles distributed on an optically flat glass surface and extracting the particle coordinates from the reconstructed images. The deviation of the measured centroids from the regressed plane provides an indication of the measurement uncertainty in the centroid positions. Figure 5 shows the probability distribution of the uncertainty obtained in this manner. The standard deviation of this distribution is about 46μm, a major part of which is due to the aberrations in the hologram and mechanical misalignments and vibrations during 3D scanning. Note that in this calibration we omit the impact due to the aberrations induced by the fluid media.

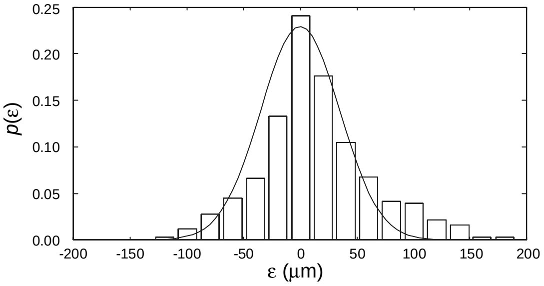

Figure 5. Calibration of particle centroid uncertainty. Totally 2251 particles are extracted. Solid line is a reference normal PDF. The overall uncertainty is 46μm.

We record eight holograms in a batch with 100ms consecutive phase delay in between. These eight phases cover one complete cycle of the vortex shedding process. On average approximately 50,000 particles are extracted for each snapshot in this measurement, out of which about 20,000 particles are individually paired to produce velocity vectors. Note that this result is actually worse than our previous experiment reported in [14] due to the drastically increased recording distance (400mm vs. 150mm), reduced angular aperture (8.5° vs. 15°), and the use of horizontal-polarization configuration. The time interval between the double-exposure is 8ms. LDV measurements show that the free-stream flow velocity is about 60mm/sec. Therefore the mean displacement between particle images reconstructed by the hologram is about 480μm. Given the 46μm centroid uncertainty from our calibration and the discussion on the velocity uncertainty in previous section, there is approximately 9.5% relative velocity error in the paired velocity vectors. We Gaussian-interpolate the velocity onto regular grids with a core size of 0.6 IC spacing before further calculations for differentials. This Gaussian interpolation also serves as a low-pass filter to minimize the impact of the velocity uncertainty, in which on average 5 pairs participates the calculation of each vector on regular grid, reducing the relative error to 4.2%. From this interpolated data field, we calculate its vorticities and demonstrate the isosurface of one instant among the eight snapshots at a threshold of $0.5\omega_m$ in Figure 6. Better means for calculating spatial derivatives from scattered 3D data exists [26], however, for demonstration purpose this simple interpolation is sufficient. The vorticity structures shown in Figure 6 agree with previous PIV [27] and DNS [28] work.

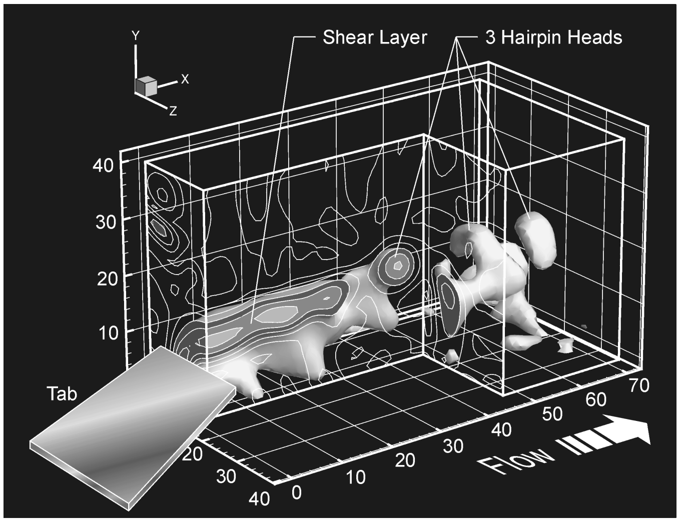

Figure 6. Vorticity isosurface from one instant. We cut out a portion of the data volume to show the inner vorticity contour. Threshold for the isosurface is $0.5\omega_m$

The choice of vorticity isosurface threshold (ω_T) to reveal vortex structures must ensure that the residue error in vorticity must be sufficiently small. Based on Equation 6, the residue divergence $|\nabla \cdot \mathbf{v}|$ can serve as an indicator of errors in vorticity. In Figure 7 (a), we plot probability density functions for the vorticity magnitude normalized by the maximum vorticity (ω_m), and the divergence magnitude in the same fashion. The statistics are from all eight snapshots. Clearly, the higher ω_T, the less significant the residue $|\nabla \cdot \mathbf{v}|$. The probability that the residue divergence (hence vorticity errors) exceeds the threshold ω_T is plotted in Figure 7 (b). The isosurface in Figure 6 is generated with $\omega_T = 0.5\omega_m$, which corresponding to approximately 2% of errors in the volume.

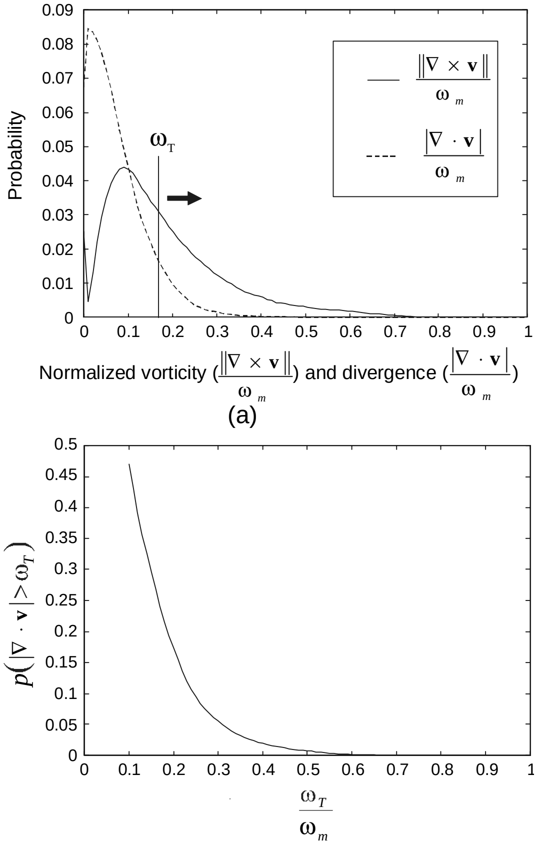

(a)

(b)

Figure 7. Statistics of divergence and vorticity from experimental data. (a) PDF of divergence and vorticity. (b) Probability of divergence exceeding vorticity isosurface threshold.

We demonstrate the whole sequence of the vorticity isosurface in Figure 8 (a)-(h). The isosurface is generated with the same threshold as that of Figure 6. Due to uneven image conditions, some of the instants may contain slightly more error among others. In Figure 8, we mark one particular coherent structure with symbol “A” to illustrate its dynamic evolution in the process. We also mark a following-up structure with “B” in Figure 8 (d)-(h). Structures A and B is identified with the aid of a video animation to reveal the correspondence of structures across the picture frames. The full dynamic process can only be best demonstrated with animated video clips.

CONCLUSION

We have addressed some fundamental issues that set the theoretical limits in the accuracy and capacity of HPIV, with examples of various possible optical configurations. We deem two physical processes, the inhomogeneous light scattering from small particles and the speckle noise in the reconstructed image, responsible for setting these limits. We presented results from our analyses with regard to critical system parameters and suggested possible methods to improve the measurements.

Though often ignored in previous research, Mie-scattering causes uneven distributions of intensity and phase, i.e. aberrations, in the wavefront the hologram records and reconstructs. Such aberrations result in systematic error and uncertainty in the location of the reconstructed particle images. Since scattering is one of the basic physical phenomena HPIV is based upon, such error is sets the primary limit in accuracy for HPIV measurements. Other practical factors, such as the emulsion shrinkage and mechanical misalignment, exacerbate the measurement accuracy but can be improved via better equipment and control. For example, an electronic holographic sensor, though not available with current technology, will completely eliminate the above two types of error. Smaller particles achieve better integrity of the reconstructed images and, hence, the measurement accuracy. Nevertheless, smaller particles require much stronger illumination to maintain the same level of scattering intensity across the hologram plane.

The intrinsic speckle noise resulted from the self-interference of the 3D dispersed particle images sets a fundamental limit for the capacity, i.e. the maximum number density of tracer particles, of HPIV. This number density determines the spatial resolution of the HPIV measurement, and therefore its applicable Reynolds number with resolution of full spectrum of structures. This speckle noise is proportional to the product of the number density of tracer particles and the depth dimension of the test volume. The capability limit of HPIV, therefore, has to be expressed in the same fashion (n_sL). Furthermore, this analysis clearly states the importance of the hologram angular aperture. Larger angular aperture drastically improves the SNR and thus the capacity of HPIV.

We have constructed a complete HPIV instrument that holds the promise of time-resolved, full-field 3D, 3C measurements. Since its first report in [14], we have further devised more advanced data processing algorithms powered by a distributed computing cluster. The lack of a film transport mechanism hinders the full deployment of this capability. However, we demonstrated the potential of the Gemini HPIV with a semi-time-series measurement for a flow passing a wall-mounted tab. Through phase-locking, the flow with the laser pulses and capturing the flow dynamics at a sequence of phases. The measurement demonstrated a full cycle of the vortex-shedding process in eight snapshots. Based on our previous analyses, we obtained detailed, quantitative specifications for the Gemini HPIV system, including measurement accuracies and dynamic ranges.

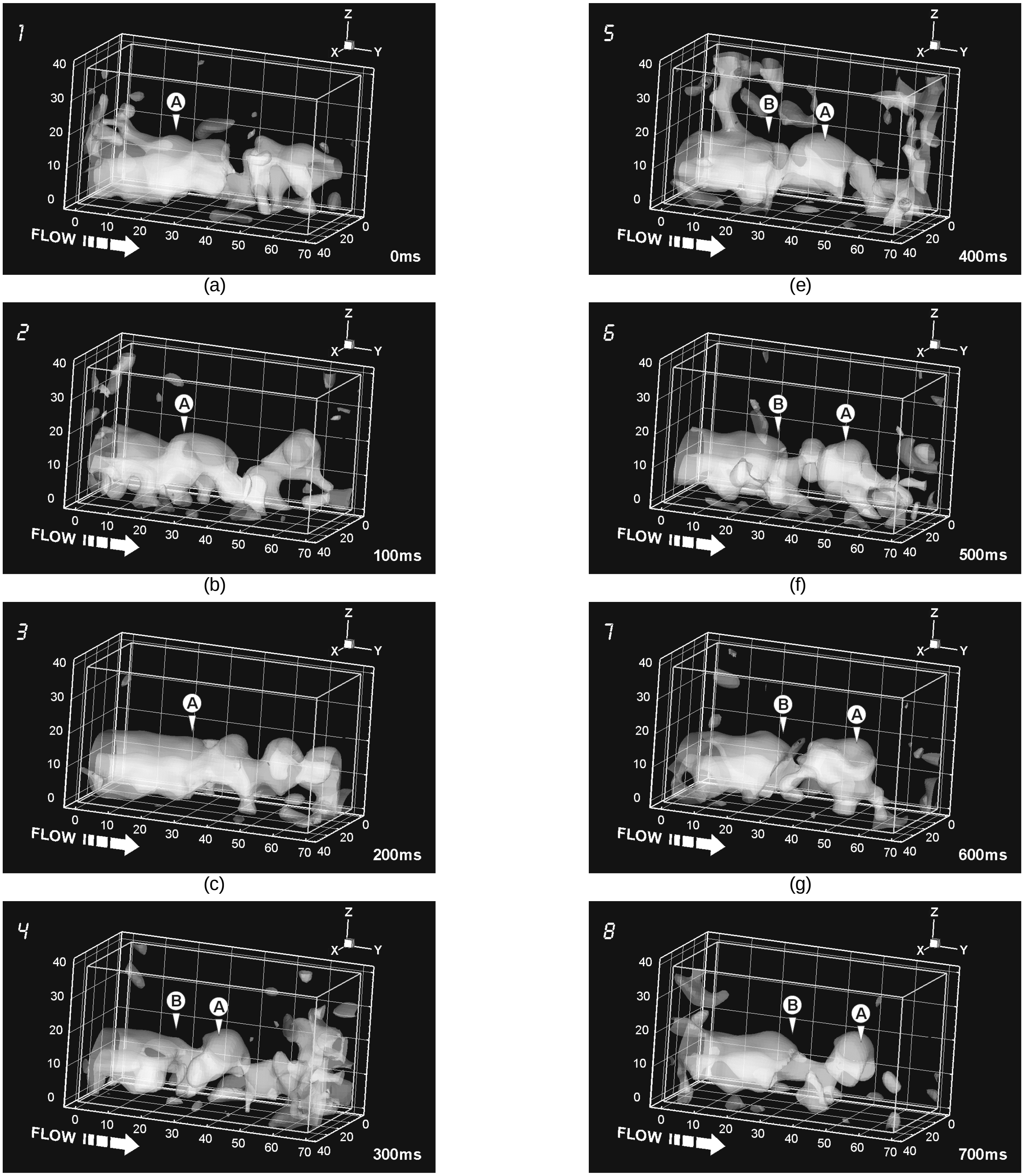

(a) (e) (b) (f) (c) (g) (d) (h)

Figure 8. A complete sequence of eight instants. Shown in the figures are vorticities extracted from the phased locked experiments. (a) 0ms. (b) 100ms. (c) 200ms. (d) 300ms. (e) 400ms. (f) 500ms. (g) 600ms. (h) 700ms.

ACKNOWLEDGEMENT

The authors wish to thank the National Aeronautics and Space Administration (NASA) for their support through grant NAG3-2464, and the National Science Foundation (NSF) for their support through grant CTS-9625307. Valuable contributions from Andrew G Bright and Scott Woodward to the experiments are greatly appreciated.

REFERENCES

1. Adrian R. J. 1991, “Particle-imaging techniques for experimental fluid mechanics”, Annu. Rev. Fluid Mech. 23, 261-304.
2. Willert C. E. and Gharib M. 1991, “Digital particle image velocimetry”, Exp. in Fluids 10, 181-193.
3. Arroyo M. P. and Greated C. A. 1991, “Stereoscopic particle velocimetry”, Meas. Sci. Technol. 2, 1181-1186.
4. Prasad K. and Adrian R. J. 1993, “Stereoscopic particle image velocimetry applied to liquid flows”, Exp. Fluids 15, 49-60.
5. Guezennec Y. G., Zhao Y., and Gieseke T. J. 1994, “High-speed 3-D scanning particle image velocimetry (3-D SPIV) technique”, Proc. Laser Symp., Lisbon, paper26.1.
6. Bruecker Ch. 1997, “3D scanning PIV applied to an air flow in a motored engine using digital high-speed video”, Meas. Sci. Technol. 8 1480-1492
7. Trolinger J. D., Belz R. A., and Farmer W. M. 1969, “Holographic techniques for the study of dynamic particle fields”, Appl. Opt. 8, 957-961.
8. Thompson B. J. 1974, “Holographic particle sizing techniques”, J. Phys. E 7, 781-788.
9. Hobson P. R. 1988, “Precision coordinate measurements using holographic recording”, J. Phys. E. 21, 139-145.
10. Meng H. and Hussain F. 1995, “In-line Recording and Off-axis Viewing (IROV) technique for holographic particle velocimetry”, Appl. Opt. 34, 1827-1840.
11. Scherer J. O. and Bernal L. P. 1997, “In-line holographic particle image velocimetry for turbulent flows”, Appl. Opt. 36, 9309-9318.
12. Meng H., Anderson W. L., Hussain F., and Liu D. 1993, “Intrinsic speckle noise in in-line particle holography”, J. Opt. Soc. Am. 10 2046-2058.
13. Barnhart D. H., Adrian R. J., Meinhart C. D. and Papen, G. C. 1994, “Phase-conjugate holographic system for high-resolution particle image velocimetry”, Appl. Opt. 33, 7159-7169.
14. Pu Y. and Meng H. 2000, “An advanced off-axis holographic particle image velocimetry (HPIV) system”, Exp. Fluids 29, 184-197.
15. Zhang J., Tao B., and Katz J. 1997, “Turbulent flow measurement in a square duct with hybrid holographic PIV”, Exp. In Fluids, 23, 373-381.
16. Lozano A., Kostas J., and Soria J. 1999, “Use of holography in particle image velocimetry measurements of a swirling flow”, Exp. Fluids 27, 251-261.
17. Barnhart D. H., Halliwell N. A., and Coupland J. M. 2000, “Holographic particle image velocimetry: analysis using a conjugate reconstruction geometry”, Opt. Laser Technol. 32, 527-533.
18. van de Hulst H. C. 1981, Light Scattering by Small Particles, Dover, New York.
19. J. W. Goodman, “Statistical properties of laser speckle patterns”, in Laser Speckle and Related Phenomena, J.C. Dainty, ed., pp. 9-75 (Springer-Verlag, Berlin, 1975).
20. Panton R. L. 1996, Incompressible Flow, pp. 770, John Wiley and Sons, New York.
21. Huang K., Slepicka J. and Cha S. S. 1993, “Cross-correlation of three-dimensional images for three-dimensional three-component fluid velocity measurements”, SPIE 2005, 655-666.
22. Pu Y., Song X., and Meng H. 2000, “Off-axis holographic particle image velocimetry for diagnosing particulate flows”, Exp. Fluids 29, S117-128.
23. Pu Y. and Andresen D. 1999, “Distributed Processing for Cinematic Holographic Particle Image Velocimetry”, Proc. 8th IEEE Int’l. Symp. on High Performance Distributed Computing (HPDC8), Los Angeles, CA, 343-344.
24. Sholes K. and Farrell P. V. 2000 “Optical alignment-induced errors in holographic particle image velocimetry”, Appl. Opt. 39, 5685-5693.
25. Bjelkhagen H. I. 1995, Silver-Halide Recording Materials for Holography and Their Processing, Springer-Verlag, Berlin.
26. Stüer H. and Blaser S. 2001, “Assessment of spatial derivatives determined from scattered 3D PTV data”, Exp. Fluids 30, 492-499.
27. Yang W., Meng H., and Sheng J. 2001, “Dynamics of hairpin vortices generated by a mixing tab in a channel flow”, Exp. Fluids 30, 705-722.
28. Dong S. and Meng H., “Direct numerical simulation of the mixing tab flow”, submitted to J. Fluid Mech.